- Structural perspective on revealing heat dissipation behavior of CoFe₂O₄-Pd
- nanohybrids: A great promise for magnetic fluid hyperthermia
- S. Fatemeh Shams, 1, * Mohammad Reza Ghazanfari, 2 Susanne Pettinger, 3,4,5 Amir H. Tavabi, 6
- Konrad Siemensmeyer, Alevtina Smekhova, Rafal E. Dunin-Borkowski, Gil G. Westmeyer, 3,4,5
- Carolin Schmitz-Antoniak¹
- 1. Peter-Grünberg-Institut (PGI-6), Forschungszentrum Jülich, 52425 Jülich, Germany
- ^V 2. Institute of Chemistry and Biochemistry, Freie Universität Berlin, 14195 Berlin, Germany
 - 3. Institute of Biological and Medical Imaging, Helmholtz Zentrum München, 85764 Neuherberg, Germany
 - 4. Institute of Developmental Genetics, Helmholtz Zentrum München, 85764 Neuherberg, Germany
 - 5. Department of Nuclear Medicine, TUM School of Medicine, Technical University of Munich, 81675 Munich, Germany
 - 6. Ernst Ruska-Centre for Microscopy and Spectroscopy with Electrons and Peter Grünberg Institut, Forschungszentrum Jülich, 52425 Jülich, Germany
 - 7. Helmholtz-Zentrum Berlin für Materialien und Energie, 14109 Berlin, Germany

Present address: Helmholtz-Zentrum Berlin für Materialien und Energie, 12489 Berlin, Germany

*Corresponding author:

19 Dr. S. Fatemeh Shams

Y · E-mail: f.shams@fz-juelich.de

Phone: +49 30 8062 14779

by adjusting the synthesis parameters.

77 77 75

70

۲٦

۳ ٤

30

۲١

٨

٩

١.

۱۳

١٤

10

١٧

Abstract

colloidal suspensions are investigated as a function of particle size, fluid concentration and magnetic field amplitude. The specific absorption rate (SAR) is found to vary with increasing particle size due to a change in dominant heating mechanism from susceptibility to hysteresis and frictional loss. The maximum SAR is obtained for particle diameters of 11-15 nm as a result of synergistic contributions of susceptibility loss, including Néel and Brownian relaxation and especially hysteresis loss, thereby validating the applicability of linear response theory to superparamagnetic CFO nanoparticles. Our results show that the ferrofluid concentration and magnetic field amplitude alter interparticle

Loss mechanisms in fluid heating of cobalt ferrite (CFO) nanoparticles and CFO-Pd heterodimer

Despite the paramagnetic properties of individual palladium nanoparticles, CFO-Pd heterodimer suspensions were observed to have surprisingly improved magnetization as well as SAR values, when

interactions and associated heating efficiency. The SAR of the CFO nanoparticles could be maximized

- compared with CFO ferrofluids. This difference is attributed to interfacial interactions between the
- magnetic moments of paramagnetic Pd and superparamagnetic/ferrimagnetic CFO. SAR values
- measured from CFO-Pd heterodimer suspensions were found to be 47-52 W/g_{Ferrite}, which is up to a
- factor of two higher than the SAR values of commercially available ferrofluids, demonstrating their
- potential as efficient heat mediators. Our results provide insight into the utilization of CFO-Pd
- heterodimer suspensions as potential nanoplatforms for diagnostic and therapeutic biomedical
- applications, e.g., in cancer hyperthermia, cryopreserved tissue warming, thermoablative therapy,
- A drug delivery and bioimaging.
- **Keywords:** heterodimers; ferrofluid heating; magnetic loss; magnetocrystalline anisotropy; interfacial
- interactions.

1. Introduction

- Magnetic fluid hyperthermia (MFH) is a promising new theranostic approach to synergistically
- improve efficacy in a wide range of biomedical applications, including controlled thermal therapy of
- cancer, cellular magnetic activation (magneto-genetics), magnetic targeted drug delivery and the
- 10 adjustment of glucose metabolism and the neuronal activity of cells [1-3]. Magnetic ferrite
- nanoparticles have attracted the most attention because of their biocompatibility,
- superparamagnetic behavior, strong magnetization (M) and effective anisotropy (K). Cobalt ferrite
- (CFO) nanoparticles, in particular, exhibit significant heat-generation ability as a result of their higher
- magnetocrystalline anisotropy [4] when compared with other ferrites.
- Y. CFO nanoparticles can be delivered to targeted tissues/organs by direct infusion into cancerous
- tissues or initial intravenous infusion and subsequent magnetic guidance to a tumor using DC
- magnetic field gradients. Local magnetic heating of nanoparticles (up to 43 °C) using an AC magnetic
- field is used to selectively damage cancerous cells in their direct vicinity. In addition, there may be
- beneficial effects for blood flow and for conventional cancer therapies [5]. For example, an
- improvement in blood supply by heating increases the efficiency of chemotherapy, while for

- temperatures above 40 °C the ability of cancerous cells to repair radiation damage is severely
- decreased, significantly increasing tumor regression in radiation therapy. The heat generation ability
- of magnetic nanoparticles can also be used for targeted drug delivery applications. For example,
- during liposomal drug delivery by magnetic nanoparticles local heat generation can be used to trigger
- the release of an encapsulated drug by the activation of a thermal release mechanism, which
- improves the drug release rate [6].
- \forall Although the generation of heat can be regulated by the amplitude (H) and frequency (f) of the
- A applied magnetic field, a practical safety limit should be observed to avoid possible adverse
- 9 phenomena, such as additional non-localized heating in the body by eddy currents during clinical
- 1. treatment [7,8]. The heat-generation efficiency should therefore be improved by tailoring the
- properties of nanoparticles, such as their size, chemical composition, structural and magnetic
- properties, as well as their biocompatibility. The size of a nanoparticle directly influences its
- crystallinity, stability, biocompatibility and magnetic properties, e.g., its superparamagnetic limit. In
- 15 addition, the ferrofluid concentration affects heat generation, agglomeration and the cell-
- cytotoxicity of nanoparticles [9].
- Since the magnetic responsivity of nanoparticles decisively influences possible applications in
- magnetic hyperthermia, there were several intense research efforts during the past years to develop
- new approaches including the design of magnetic nanoparticles with non-spherical shapes such as
- cubic, flower-shape, and elongated particles [10]. For non-spherical particles, the total magnetic
- anisotropy is enhanced due to the additional shape anisotropy. Furthermore, two-phase magnetic
- nanoparticles consisting of a magnetic core and a non-magnetic shell could provide a higher heat
- generation, although in many cases the total mass magnetization is significantly decreased [10]. In
- some other cases, agglomeration of nanoparticles to larger magnetic clusters could increase the heat
- generation ability, but limits their use for in vivo applications.

- Colloidal hybrid nanoparticles with diverse structures, such as mosaic, core-shell, multi-core-shell and
- heterodimer, act as multipurpose agents for biomedical applications [10]. Among these structure
- models, heterodimers of CFO nanoparticles and noble metal particles of palladium (Pd) have been
- recognized as efficient multifunctional agents for potential biomedical purposes, including
- photothermal therapy, cell separation and optical tracking of therapeutic agents [11-13]. However,
- the relatively poor heat transfer efficiency of CFO necessitates the use of a highly concentrated
- Y ferrofluid for effective hyperthermia treatment, which inhibits its practical utilization in clinical
- h treatments [14-17].
- ⁹ In addition, there are some concerns about the biocompatibility of CFO nanoparticles but several
- studies introduce CFO nanoparticles as a promising candidate for bioapplications [18-21].
- Additionally, it is experimentally confirmed that the CFO nanoparticles could effectively inhibit the
- proliferation of carcinoma cells [22].
- There are two general approaches to further improve the biocompatibility of CFO: The first is based
- on covering the magnetic cores through biocompatible ceramic/polymeric shells such as silica, PVA,
- PEG, and citrate [23,24]. The second is based on the synthesis of CFO substituted with biocompatible
- metals like Ag or Cu [25]. However, in both cases, the total magnetization might be negatively
- ۱٧ affected.
- In contrast to most diamagnetic noble metals, such as Cu, Ag and Au, Pd is a paramagnet with a large
- magnetic susceptibility. Ultrasmall paramagnetic Pd nanoparticles may exhibit even enhanced
- magnetic properties [26] compared to the corresponding bulk material and can maintain the basic
- net magnetic features of CFO, accompanied by emerging new optical properties. Moreover, the
- biocompatibility and physicochemical stability of Pd nanoparticles result in the formation of
- biocompatible CFO-Pd heterodimers [27].
- The fabrication and magnetic characterization of nano-hybrids consisting of magnetic nanoparticles
- and noble metals with different morphological structures, such as core-shell, phase segregated and

- heterodimers, have been discussed [28-38]. However, a study of the magnetic heat generation ability
- of CFO-Pd heterodimers has not yet been reported.
- In the present work, the dominant mechanisms of magnetic heat generation of CFO nanoparticles
- upon application of an alternating magnetic field are studied by the experimental measurement of
- the specific absorption rate (SAR). The effects of particles size, ferrofluid concentration magnetic
- field amplitude on the heat-generating ability of CFO nanoparticles are investigated. Furthermore,
- magnetic features and the associated heat generation properties of CFO-Pd heterodimers in two
- A different ranges of particles size are characterized and discussed. Correlations between SAR value
- and structural factors, i.e. degree of crystallinity, crystallite size and cation distribution in CFO, are
- evaluated and optimized. To the best of our knowledge, there have been no previous studies of the
- magnetic and heat-generating properties of CFO-Pd heterodimers. Accordingly, this is the first
- investigation of CFO-Pd hybrid architectures for use in magnetic hyperthermia biomedical
- 17 applications.

۲١

2. Experimental Section

10 2.1. Chemicals

- In order to synthesize CFO nanoparticles, precursors consisting of FeCl₃.6H₂O and CoCl₂.6H₂O (>99%,
- Merck) as magnetic cation resources, NaOH (1 M, Merck) as an adjusting agent of the solution pH,
- and citric and nitric acids (>99.5%, >65%, Merck) as chelating agents, were employed. Materials for
- preparing CFO-Pd heterodimers structures included PdCl₂ (>99%, Merck), KCl (>99.5%), HCl (37-38%)
- and citric acid. All materials, solutions and surfactants were used without any further purification.

2.2. Synthesis of CFO Nanoparticles and CFO-Pd Nano-Heterodimers

- Superparamagnetic CFO nanoparticles were synthesized using a modified coprecipitation method.
- The pH of a mixture solution of Fe and Co chloride salts was adjusted using NaOH solution (1 M) to
- prepare the required condition for magnetic ferrite phase reduction. The size of the synthesized CFO

particles was controlled by the reaction temperature, which was selected according to the design of experiments approach. Citric and nitric acids were used as chelating agents to control the size, size distribution and physical stability of the nanoparticles, which were dispersed in a colloidal ferrofluid after magnetic separation and washing progressions. Further information about the CFO nanoparticle synthesis process is provided in our previous works [39,40]. In order to randomly attach metallic Pd nanoparticles to CFO nanoparticles and create CFO-Pd heterodimers, 2 vol.% of HCl solution was added and sonicated for 20 min. to disperse the agglomerated CFO clusters and activate their surfaces to connect with the ultrasmall Pd particles. Mixing of the PdCl₂ and KCl salts in aqueous medium for 30 min. led to the formation of a water-soluble intermediate phase of K₂PdCl₄. After adding CFO nanoparticles and homogenizing for 60 min. at room temperature, the pH of the medium was regulated to be in the range 12-13 using NaOH solution. The resulted colloidal solution was incubated for 24 h with controlled nitrogen flow. The resulting samples were centrifuged, magnetically separated, washed with ethanol and deionized water, pH-naturalized and dried at ambient temperature using a vacuum dryer.

2.3. Characterization

١.

۲.

The sizes and structures of the synthesized CFO nanoparticles were characterized using dynamic light scattering (DLS, MALVERN, Zetasizer Nano ZSP) and X-ray diffraction (XRD, Bruker Advance 2), respectively. Characterization of the microstructural and elemental features of the CFO nanoparticles and CFO-Pd heterodimers was carried out using high-resolution scanning transmission electron microscopy in high-angle annular dark-field mode (HAADF-STEM, FEI Titan G2 80-200 ChemiSTEM) [41], and energy dispersive X-ray spectroscopy (EDS, Titan G2 80-200 ChemiSTEM) at a primary energy of 200 keV. Magnetic properties were measured using a vibrating sample magnetometer (VSM, VSM-PPMS-14T) at up to 13 T and ambient temperature (300 K).

2.4. Magnetic Fluid Heating and SAR Measurement

In order to study magnetic fluid heating, ferrofluid temperature variations as a function of time were measured at constant volume (1 ml for all samples) at different concentrations in the presence of an AC magnetic field with H = 19 mT (I = 33 A) and f = 318 kHz. In order to assess the effect of the magnetic field amplitude, some experiments were also conducted at H = 12 mT (I = 22 A). All of the measurements were performed at ambient temperature and atmosphere using a *TruHeat HF 3010* system equipped with a fiber-optic temperature probe. The four-turn induction coil had a total height of approximately 6 cm and an inner diameter of 10 cm. In order to eliminate the effect of a different starting temperature, curves were initially plotted (Fig. 3) as a function of temperature difference (ΔT) and the magnetic field was applied after fixing the indicated probe temperature. The SAR factors of the samples were calculated based on the well-established equation [42]

١.

$$SAR = C \times \left(\frac{\Delta T}{\Delta t}\right) \times \left(\frac{m_S}{m_F}\right),\tag{1}$$

where C is the specific heat of water (4.184 JK^1g^{-1}), ($\Delta T/\Delta t$) is the initial slope of the temperature vs time curve, m_s is the mass of the sample and m_F is the mass of ferrite, which is equal to the total mass of the magnetic cations and oxygen anions in the bare CFO samples and the total mass of the magnetic cations, oxygen anions and Pd nanoparticles in the CFO-Pd samples. The total mass of CFO (or CFO + Pd) is only preferred over the total mass of magnetic cations in SAR calculations to achieve more realistic values for applications.

The change in temperature with time is related to the dissipated power P according to the well-known relation

$$P = m_S C\left(\frac{\Delta T}{\Delta t}\right). \tag{2}$$

In this regard, the SAR can be understood as the dissipated power per mass of magnetic material (here, CFO). For magnetic heating by superparamagnetic particles in an AC magnetic field, the dissipated power depends on external factors, such as magnetic field amplitude *H* and frequency *f*, as

- well as internal factors, such as the imaginary part of the AC magnetic susceptibility χ'' and the
- τ effective relaxation time τ , according to the equations [43]

$$\chi'' = \frac{\omega \tau}{1 + (\omega \tau)^2} \chi_0 \tag{3}$$

$$P = \mu_0 \pi \chi'' f H_0^2 = \pi \mu_0 \chi_0 H_0^2 f \frac{2\pi f \tau}{1 + (2\pi f \tau)^2}, \tag{4}$$

- where ω is the angular frequency $f=rac{\omega}{2\pi}$, χ_0 is the equilibrium susceptibility, H_0 is the small applied
- $^{\text{T}}$ $\,$ field and $\mu_0 = 4\pi \times 10^{-7}$ T m $\text{A}^{\text{--}1}$ is the vacuum permeability.
- In order to explore the effective influence of size and concentration of the CFO nanoparticles, as well
- A as the amplitude of the magnetic field, on heat generation, several experimental runs were
- 9 performed. The characteristics of the sample series that were used to evaluate the size,
- v concentration, and field amplitude dependent SAR factors of bare CFO and CFO-Pd architectures are
- presented in the Supplementary Information (Tables S1, S2 and S3). In all of the MFH measurements,
- the approximate uncertainty is 2%.

2.5. Optimization

۱۳

۲١

- Optimization studies were carried out based on the central composite design (CCD) approach of
- response surface methodology (RSM) using the DESIGN EXPERT software program to understand the
- correlation between SAR values and structural factors, such as crystallite size, degree of crystallinity
- and cation disorder. Predictor models were used to determine optimal values of different factors to
- achieve the targeted responses. More details about the samples, as well as the optimization process,
- are presented in the Supplementary Information.

7. 3. Results and Discussion

3.1. Structural Characterization and Magnetometry

- The first step in the preparation of CFO-Pd heterodimers and studies of their magnetic fluid heating
- was the synthesis of CFO nanoparticles with controlled sizes, size distributions and crystal structures.

١ Results of X-ray diffraction (XRD) analyses (Figure S1 in the Supplementary Information) confirmed ۲ the formation of nanoparticles with an inverse spinel structure of the cobalt ferrite phase CoFe₂O₄, ٣ without the detectable formation of undesirable hydroxide or oxide phases such as CoO. ٤ Quantitative analyses of the XRD results using Rietveld structure refinement confirmed the ٥ crystallization of nanoparticles in the target phase with a significant degree of crystallinity (>85%). ٦ Crystallite sizes calculated from Pseudo-Voigt profiles showed acceptable correspondence with ٧ particles sizes measured using dynamic light scattering (DLS) and microscopic approaches. The ٨ hydrodynamic size d_H, size distribution D_V and polydispersity index (PDI) of the synthesized ٩ nanoparticles were obtained using DLS. Based on the results (Table S1), the mean hydrodynamic ١. diameters of particles in the different samples were determined to be between 7.2 and 40 nm with a 11 narrow distribution, while the corresponding crystallite diameters d_{Cryst} varied between 5.8 and ۱۲ 32.2 nm. The hydrodynamic PDI values of all of the samples were below 0.1, indicating the suitability ۱۳ of the nanoparticles for use in biomedical and especially in vivo applications [44]. ١٤ In the next step, the formation of CFO-Pd heterodimers as novel hybrid nano-architectures was 10 evaluated using microscopic analysis. Figure 1 shows high-angle annular dark-field scanning ١٦ transmission electron microscopy (HAADF-STEM) micrographs of CFO-Pd nanostructures obtained ١٧ from suspension. The mean diameters of the CFO and Pd nanoparticles are approximately 7 and ١٨ 2 nm, respectively, with a PDI value of 0.07. Morphologically, the nanoparticles are uniform and 19 close-to-spherical. Crystalline CFO nanoparticles with attached ultrasmall Pd particles are clearly ۲. visible in the STEM images. Element-specific mapping of the CFO-Pd nanostructures was performed ۲١ using energy-dispersive X-ray spectroscopy (EDS), as shown in Fig. 2. The CFO nanoparticles contain ۲۲ Fe, Co, and O, while Pd is visible in the attached particles. ۲۳ Magnetometry measurements recorded in applied magnetic fields of up to 13 T at a temperature of ۲٤ 300 K are shown in the Supplementary Information (Fig. S2) for bare CFO nanoparticles with two 70 different hydrodynamic diameters (7.2 and 24.1 nm) and for corresponding CFO-Pd heterodimers.

Vanishing coercivity (\leq 5 mT) and remanence (\leq 4-6% of the saturation magnetization (M_s)) are

indicative of a primarily superparamagnetic state. Even in high external magnetic fields of 10 T and above, magnetic saturation was not reached. The high-field data, *i.e.* magnetometry data in fields of above 3 T, were fitted to the law of approach, as shown in the Supporting Information (Fig. S2 and Table S4) and the effective magnetic anisotropy was extracted from the fitting parameters. In addition, the magnetic DC susceptibility was analyzed. The results are summarized in Table 1. For both nanoparticle sizes, the high-field magnetization, effective anisotropy and low-field susceptibility were significantly enhanced upon Pd decoration. These effects were more prominent for smaller CFO nanoparticles. The magnetometry results further motivate the investigation of magnetic heating properties for bare and Pd-decorated CFO nanoparticles of different sizes.

3.2. Specific Absorption Rates

۲.

۲ ٤

AC Magnetic Field Amplitude-Dependent Fluid Heating

In order to obtain a better understanding of the effect of magnetic field amplitude, SAR values were measured from samples with a constant concentration of 15 mg/ml for three different ranges of particle hydrodynamic diameters (10.24, 13.70 and 17.77 nm) in applied magnetic fields with amplitudes of 12 and 19 mT (and currents of 22 and 33 A, respectively). The frequency f = 318 kHz was constant. The product $H \cdot f$ was below the safety limit for both amplitudes (3.0 × 10⁹ and 4.8 × 10⁹ $Am^{-1}s^{-1}$, respectively) and appropriate for *in vivo* biomedical applications [45]. The resulting field-amplitude-dependent SAR values are given in the Supplementary Information (Fig. S3). The dissipated power and, as a consequence, the SAR values of all of the samples decreased considerably for smaller magnetic field amplitudes, are in agreement with previous studies [46,47].

Since the magnetic susceptibility is field-dependent (Fig. S4) and a ferromagnetically blocked fraction of nanoparticles is present, in particular for the larger particles, there are deviations from a simple H^2 dependence. As a minor additional effect, the effective relaxation time may be changed as a result of magnetic dipolar interactions between the particles, which depend on the field-dependent magnetic

moments. Further experiments were carried out with AC magnetic field amplitudes of 19 mT, for which the larger SAR values were obtained.

Particle-Size-Dependent Fluid Heating

٣

۱۲

۱۳

١٤

10

١٦

١٧

١٨

19

۲.

۲۳

۲٤

٤ All particle-size-dependent measurements were carried out on samples with the same concentration ٥ (15 ml/mg) in the presence of an AC magnetic field with H = 19 mT and f = 318 kHz. The measured ٦ temperature variation as a function of time ($\Delta T/\Delta t$) is shown in Fig. 3a. The temperatures of all of the ٧ samples were raised to 43 °C, the desired temperature for hyperthermia, in reasonable times (less ٨ than 15 minutes), confirming the potential effectiveness of CFO nanoparticles for thermal therapy ٩ applications. Figure 3b shows the initial slopes of the $\Delta T/\Delta t$ curves and corresponding fitted linear ١. equations to calculate SAR values. The difference in heat-generation ability of the different samples 11 within the first two minutes of the measurements is clearly visible.

The extracted SAR values as a function of mean hydrodynamic particle diameter are shown in Fig. 4a. The variation in particle size leads to irregular changes in SAR factor, meaning that two SAR peaks are observed for particle hydrodynamic diameters of 12.05 and 14.77 nm. The activation of different heat loss mechanisms in different size ranges can result in such features in the dependence of SAR value on nanoparticle size. Increasing the particle hydrodynamic diameter from 7.2 to 40 nm activated different loss mechanisms sequentially, including susceptibility (Néel and Brownian relaxation), hysteresis and frictional losses as the dominant mechanisms. In order to estimate the size dependence of the different relaxation channels, Néel and Brownian relaxation times were calculated based on the equations [9,48]

$$\tau_N = \tau_0 e^{\left(\frac{KV}{k_B T}\right)} \tag{5}$$

$$\tau_B = \left(\frac{4\pi\eta r_H^3}{k_B T}\right),\tag{6}$$

where τ_N is the Néel relaxation time, τ_B is the Brownian relaxation time, $\tau_0 = 10^{-9}$ s [46,47,49], V is the geometric volume of the nanoparticle, K is the effective anisotropy, k_B is the Boltzmann constant, T is

the measurement temperature, η is the viscosity of the ferrofluid and r_H is the hydrodynamic radius of the nanoparticle. The effective relaxation time was calculated from the Néel and Brownian relaxations using the expression

$$\tau_{eff} = \frac{\tau_N \times \tau_B}{\tau_N + \tau_B} \,. \tag{7}$$

٥

٦

٧

٨

٩

١.

11

۱۲

۱۳

١٤

10

١٦

١٧

١٨

19

۲.

۲١

۲۲

۲۳

Figure 4b shows the Néel, Brownian and effective relaxation times plotted as a function of particle hydrodynamic diameter. Initially, in the range of small particle diameters up to 11 nm, the dominant mechanism of heat generation is Néel relaxation loss. Further augmentation of particle size changes the dominant mechanism into Brownian relaxation loss, reaching a maximum SAR value at a particle diameter of approximately 12.05 nm. For particle sizes above the superparamagnetic dimension D_{S} , the dominant mechanism is hysteresis loss. The size-dependent heating trends and associated dominant mechanisms are consistent with linear response theory (LRT) for superparamagnetic nanoparticles and the Stoner-Wohlfarth model of hysteresis for ferrimagnetic structures [50]. Néel relaxation loss in smaller nanoparticles is associated with a rotation of the magnetic moments inside them, while Brownian relaxation depends on the ferrofluid viscosity, as it is associated with particle rotation in a fluid medium [51]. The dominant mechanism of magnetic heat generation changed from Néel to Brownian relaxation loss with increasing particle diameter, followed by a subsequent increase in fluid viscosity. Ferrimagnetic states and corresponding hysteresis loops were formed in particles with sizes larger than D_s , with hysteresis loss identified as the dominant mechanism with increasing particle size [5], in accordance with the dynamic hysteresis model (DHM), as a result of an enhancement in their magnetization and magnetic anisotropy [1]. The area of influence of each mechanism could be distinguished in the particle-size-dependent SAR variation curve. In order to determine the dominant loss mechanism, the critical diameter of susceptibility loss limit, D_{Sus} , in zero/small magnetic field is given by the equation [46]

$$D_{Sus} = \left[\frac{6 k_B T \ln (f_m \tau_0)}{\pi K}\right]^{\frac{1}{3}}, \tag{8}$$

where f_m is the measurement frequency (here, 318 kHz). Since the particles are ferromagnetically

blocked above this critical diameter and the dominant loss mechanism changes from susceptibility to

hysteresis loss, it corresponds to D_s . The critical diameter for our samples is 13.66 nm, which helps to

é explain the size-dependent SAR peaks.

A shoulder on the first SAR peak at approximately 11 nm is attributed to the maximum efficiency of

Néel relaxation loss. An increase in particle size leads to a gradual decrease in the effectiveness of

Néel loss and to the development of Brownian relaxation as the dominant loss mechanism. The

Brownian mechanism efficiency is maximized at the utmost point of the SAR first peak at

approximately 12.05 nm. Although the areas of influence of these mechanisms overlap each other,

only one of them is dominant in each size range. An increase in particle size up to the ferrimagnetic

range leads to a dramatic weakening of the relaxation loss mechanisms and associated SAR values.

Above a particle size of 13.67 ± 0.5 nm (from Eq. 8), the dominant mechanism changed to hysteresis

loss and the SAR value increased with particle diameter. Accordingly, two pronounced SAR values

were detected in the size ranges 14-15 nm and 11-12 nm, in order of intensity. The SAR value was

gradually reduced with increasing particle diameter, especially above 17 nm, due to the insufficient

field amplitude (19 mT) to switch the magnetic moments of larger particles [46]. In this particle size

range, frictional loss is likely to be the dominant heating mechanism because of fluid viscosity

• enhancement.

٦

٨

٩

١.

11

۱۲

۱۳

١٤

10

١٦

١٧

19

۲.

۲١

۲۲

۲۳

۲٤

70

۲٦

CFO Concentration-Dependent Fluid Heating

In order to achieve a better understanding of the influence of ferrofluid concentration on the magnetic heating of CFO nanoparticles, SAR values were measured for samples with different particle diameters for both low and high concentrations (approximately 1 and 15 mg/ml, respectively) in applied magnetic fields with H = 19 mT and f = 318 kHz. Figure 5 shows measured SAR values of CFO samples with five different hydrodynamic particle diameters for the two different concentrations. In all of the analyzed samples, the SAR values decreased dramatically (by more than 50%) at high concentrations, probably because of particle agglomeration and inter-particle dipolar interactions

(IPDI), such that the superparamagnetic properties of particles almost vanished, the Néel and in particular the Brownian relaxation mechanisms were weakened and the SAR values were reduced [52-54]. The inter-particle distance could be decreased in highly-concentrated fluids, leading to a bulk-like state performance and to the activation of hysteresis and frictional losses as the dominant mechanisms of fluid heating [55-57]. Whereas the susceptibility loss vanished for the highlyconcentrated samples, the hysteresis loss had a small contribution at H = 19 mT to fluid heating for highly-concentrated particles in agglomerated assemblages. The inverse proportionality of IPDI strength and remanence ratio M_r/M_s had been confirmed both theoretically and experimentally [58-63], while the hysteresis loss was affected strongly by the remanence ratio. Although the results about the effect of concentration were obtained from samples with specific nanoparticle sizes and cannot be generalized to all particle size intervals in size-dependent SAR values, including the maximum peaks, the analogous SAR variations of measured low- and high-concentrated samples (in five ranges of particle size) increase the probability of a similar trend over all size ranges, including the maximum SAR values. With reference to Fig. 5, although the time required for the fluid to reach the temperature needed for successful hyperthermia treatment was shortened for the highly-concentrated suspensions (corresponding to a sharper $\Delta T/\Delta t$ slope), their heating efficiency was lower. As a result of the unpleasant effects of using a high concentration on the biocompatibility and superparamagnetic behavior of the fluids, the use of low-concentration samples has an important role in biomedical applications [14]. In order to obtain an understanding of the reproducibility of the measurements and its influence on fluid heating, the SAR values of CFO ferrofluids with four different ranges of particle diameters (11.04, 12.17, 14.77 and 15.70 nm) were obtained from repeated measurements performed for the same concentrations of 15 mg/ml and magnetic field amplitudes of 19 mT. SAR values obtained from the first and second runs of measurements varied slightly for all of the samples, as a result of the enhancement of viscous and isothermal remanent magnetizations (VRM and IRM, respectively)

١

۲

٣

٤

٥

٦

٧

٨

٩

١.

11

۱۲

۱۳

١٤

10

١٦

١٧

١٨

19

۲.

۲١

۲۲

۲۳

۲٤

70

during repeated measurements [64]. The results are presented in the Supplementary Information

(Fig. S5). Whereas the SAR values decreased in the second run for the two smallest diameters, they

increased for the larger diameters. A critical diameter D_S may be introduced, with D_S = 12.5-14.5 nm,

which is consistent with the value calculated from Eq. 8. For single-domain ferrimagnetic

nanoparticles with $d > D_S$, the primary loss mechanism leading to magnetic heating is hysteresis loss,

which is increased by contribution from IRM and especially VRM in repeated runs of measurements,

leading to improved SAR values. For smaller particles with $d < D_S$, an increase in remanent

magnetization attenuates relaxation losses, particularly those related to the Brownian mechanism,

leading to negative SAR differences in samples with particle sizes of 11.04 and 12.17 nm.

Magnetic Heating of CFO-Pd Ferrofluids

١.

۲.

In order to obtain a detailed understanding of the influence of Pd decoration on the magnetic heating of CFO ferrofluids, SAR values of heterodimer CFO-Pd hybrid nanoparticles were monitored for two different ranges of CFO particle size and a constant Pd concentration of (2 ± 0.5) wt%. All of the measurements were performed for the same ferrofluid concentration (1 mg/ml) and magnetic field (H = 19 mT, f = 318 kHz). Figure 6 shows measurements of SAR values for bare and Pd-decorated CFO nanoparticles with mean hydrodynamic diameters of 7.20 and 24.10 nm. In both sample series, the measured SAR values increased after Pd decoration. This effect was most significant for the larger particles. Although the initial SAR value of the larger bare CFO nanoparticles (24.10 nm) was lower than that of the smaller nanoparticles (7.20 nm), after Pd decoration the larger particles showed higher SAR values.

Interactions between the magnetic moments of the ultrasmall paramagnetic Pd and CFO nanoparticles can create a spin-glass-like state [65-67]. The Pd structures can then pin or freeze the ordered moments of the magnetic core, ameliorating the SAR values, particularly for larger particles. This mechanism does not affect relaxation losses, which originate at the interfaces of the Pd and CFO structures. Magnetic coupling between the Pd moments and the canted surface spins of the CFO nanoparticles improves the effective anisotropy and increments the SAR values [68,69], in agreement

with anisotropy values determined from magnetometry (Table 1). In order to further explain these observations, the magnetometry results are discussed in more detail. We follow the approach of introducing a spin disorder layer t_d according to the expression [70]

$$t_d = d \cdot \frac{1 - \left(\frac{M_S}{M_S^{bulk}}\right)}{6},\tag{9}$$

١.

۲.

where d is the mean nanoparticle diameter, M_S is the saturation magnetization of the nanoparticles and M_S^{bulk} is the saturation magnetization of cobalt ferrite in its bulk state (90 $emu.g^{-1}$) [71-73]. Based on this relation, the thickness of the spin disorder layer decreases from 3.3 to 2.7 nm for the larger CFO particles and from 1.1 to 0.8 nm for the smaller CFO particles upon decoration with Pd. These results suggest that the relative thickness of the spin disorder layer t_d/d exhibits a non-linear inverse proportionality relationship to the SAR value of the samples.

Figure 7 shows the magnetic anisotropies of bare and Pd-decorated CFO samples. After Pd decoration, the anisotropy values of both the large and in particular the small nanoparticles increased significantly. This behavior is associated with the enhanced SAR values. This connection between magnetic anisotropy and SAR is now discussed in more detail for the two different particle sizes and their corresponding loss mechanisms. For the 7.20 nm nanoparticle suspension, combined Néel and Brownian relaxation is the dominant mechanism of fluid heating. As Néel relaxation depends directly on magnetic anisotropy (Eq. 5), the enhanced magnetic anisotropy that results from Pd decoration (Table 1) slows down Néel relaxation. The fluid viscosity of the Pd-decorated samples was also slightly augmented. As this is a critical factor for the Brownian loss mechanism (Eq. 6), it also slows down Brownian relaxation. The Néel and Brownian relaxation times - and therefore also the effective relaxation time - are larger for the CFO-Pd heterodimers, shifting the curves in Fig. 4 (lower panel) upwards. This behavior is qualitatively connected to a shift in SAR towards smaller diameters (Fig. 4, upper panel), such that the small diameter of 7.20 nm is closer to the (first) maximum SAR. The SAR value for the 7.20-nm-sized CFO ferrofluid was subsequently increased after Pd decoration.

The most effective heating mechanisms for the 24.10-nm-sized nanoparticle suspension were hysteresis loss and primarily frictional loss. By increasing the magnetic anisotropy, hysteresis loss was augmented. This effect is enhanced further by the increased remanent (and saturation) magnetization after Pd decoration and can explain the larger SAR for the 24.10 nm particles. To investigate the hysteresis loss mechanism is details, in addition to the calorimetry under AC magnetic field, the AC magnetometry and related hysteresis loop could be helpful as has been discussed for the example of the iron ferrite structure in the literature [74-76]. For all ranges of particle size, the shape uniformity of the particles decreases as a result of Pd decoration. Frictional loss, especially in larger sized nanoparticles, is then activated as the dominant heating mechanism. Frictional loss results from translational and rotational motions of the nanoparticles in the ferrofluid and magnetic forces according to the expressions [47]

$$F_t = m. \nabla H \tag{10}$$

$$F_r = m \times H, \tag{11}$$

where F_t is the transitional force, F_r is the rotational force, m is the magnetic dipole moment and H is the magnetic field. These magnetic forces are much more effective for larger nanoparticles, especially for single-domain ferrimagnetic nanoparticles, which are characterized by $d > D_S$ and whose magnetic moments are blocked.

Our results show that the SAR values of CFO-Pd heterodimers improved significantly, when compared to those of bare CFO nanoparticles, due to differences in active heating mechanisms, including Néel and Brownian relaxations, hysteresis and frictional losses. The CFO-Pd samples that we studied have significantly higher SAR values than commercial hyperthermia agents. For example, MagForce AG®, which is a pioneer commercial company in hyperthermia treatment, uses agents with SAR values of 10-40 W/g_{magnetic element} [77], whereas the CFO-Pd ferrofluid studied here has SAR values of 66-68 W/g_{magnetic element}.

3.3. Optimization

١.

۲.

۲ ٤

Given the importance of the heating ability of CFO nanoparticles for magnetic fluid hyperthermia applications, we now address the optimization of synthesis factors, including reaction temperature, initial pH and Co²⁺/Fe³⁺ cation ratio, to achieve a desired SAR value. We also make use of a correlation between SAR value and structural properties such as degree of crystallinity, cation distribution and crystallite size for optimization. More details about the influence of synthesis parameters and structural properties on the magnetic properties of nanoparticles are available in our previous works [35,36]. In order to consider the impact of cation distribution, a factor (X_B-X_A) was defined based on the following chemical formula for CFO nanoparticles:

 $(Co_{XA} Fe_{1-XA})(Co_{XB} Fe_{2-XB})O_4$.

١.

۲.

۲ ٤

Figure 8a-c shows SAR values plotted as a function of synthesis parameters. An increment in initial pH value in the range 8-12 results in significantly enhanced SAR values, as a result of a higher probability of CFO phase formation at higher pH values [39]. The SAR values area also augmented by an elevated Co²⁺/Fe³⁺ cation ratio and in particular reaction temperature, due to an increase in both the degree of crystallinity and the crystallite size of the CFO phase [39]. Among these synthesis parameters, the reaction temperature and pH have the greatest influence on the SAR value of the CFO nanoparticles, whereas the cation ratio has a minor effect.

Figure 8d-f shows SAR values plotted as a function of structural properties. Higher degrees of crystallinity of the CFO phase can be seen to improve the SAR values, whereas the influence of crystallite size depends on the degree of crystallinity. At the maximum level of crystallinity, the SAR values increase significantly on enlarging the crystallite size. An increment in cation distribution factor (X_B-X_A) leads to a gradual increase in SAR value, as a result of a change in the magnetic structures of the nanoparticles [40]. Experimental measurements can be used to predict optimized correlations for a broader range of factors. Table 2 shows optimized synthesis parameters and structural properties for achieving maximal SAR values. Upon applying an AC magnetic field with

- H = 19 mT and f = 318 kHz, the SAR value is maximized at 78.205 W/g_{CFO+Pd} by adjusting the
- temperature, pH and cation ratio to 105 °C, 10.61 and 0.52, respectively. The maximal SAR value is
- predicted for structural properties of the CFO nanoparticles of crystallite size, crystallinity and (X_B-X_A)
- factor equal to 12.67 nm, 76.32 % and 0.45, respectively.

4. Summary and Conclusions

٥

٦ A systematic study of magnetic fluid heating of CFO nanoparticles and CFO-Pd heterodimers ٧ suspensions has been presented, resulting in the introduction of new hyperthermic agents with ٨ significantly increased SAR values (by up to two times) when compared to established commercial ٩ treatment agents. Studies of the dominant loss mechanism provided an improved interpretation ١. based on a combination of the Rosensweig and dynamic hysteresis models. The measured SAR values ۱١ were found to depend on the sizes of the magnetic CFO nanoparticles, which resulted in the ١٢ activation and/or strengthening of different heat generation mechanisms, including susceptibility, ۱۳ hysteresis and frictional losses. The maximal SAR values of bare CFO nanoparticles, which were ١٤ achieved for particle diameter ranges of 14-15 nm and 11-12 nm in order of intensity, were 10 attributed to hysteresis and susceptibility mechanisms, respectively. The calculated critical limit for ١٦ susceptibility loss D_{Sus} = 13.66 nm is consistent with this interpretation and with data reported in the ١٧ literature [78,79]. Our experimental size-dependent SAR measurements validate the LRT model for ١٨ CFO nanoparticles, which is not sufficient to describe the properties of magnetic iron oxide 19 nanoparticles [1,70]. In accordance with the Rosensweig model, fluid heating of CFO nanoparticles is ۲. found to depend significantly on magnetic dipole-dipole interactions, which are influenced by the ۲١ ferrofluid concentration, magnetic field amplitude and H.f factor. Although hysteresis loss showed ۲۲ the highest SAR intensity in a size-dependent manner and represents the most effective fluid heating ۲۳ mechanism, it was found to be valid for ferrimagnetic nanoparticles characterized by $d > D_S$, which ۲ ٤ are not ideal candidates for biomedical in vivo applications because of the probability of magnetic 40 agglomeration and complications such as thrombosis [5]. For superparamagnetic nanoparticles,

- susceptibility loss, including Néel and Brownian relaxations, was the primary contributor to fluid
- heating, demonstrating optimal magnetic, hyperthermic and biological properties.
- The SAR values of CFO-Pd heterodimers were substantially improved, when compared to those of
- bare CFO nanoparticles, because of interfacial interactions between the magnetic moments of Pd
- o and CFO nanoparticles, resulting in reduced spin canting, stronger internal fields and enhanced
- anisotropy without any substantial effect on the relaxation mechanisms. The calculated SAR values of
- V CFO-Pd heterodimer suspensions were 47-52 W/g_{Ferrite}, which are higher than the best-reported
- A values in commercially available ferrofluids [77]. These findings present an important insight into the
- q utilization of hybrid nanostructures of CFO-Pd heterodimers with excellent time-dependent
- temperature enhancement for biomedical applications.

- Author Contributions: Conceptualization and design, S.F.S.; Synthesis and preparation of samples,
- S.F.S.; SAR measurements, S.P.; STEM-HAADF Microscopy measurements, A.H.T.; Analysis and
- discussion of the results, S.F.S., C.S.A., M.R.G. and A.S.; Writing original draft preparation, S.F.S. and
- M.R.G.; Writing review and editing, S.F.S., M.R.G. and C.S.A.; Project leadership, C.S.A.; Project
- administration, S.F.S. and C.S.A.; Supervision, C.S.A., G.G.W. and R.E.D.B.; All authors read, discussed,
- v commented and approved the final manuscript.
- 14 Funding: Parts of this research were funded by the Helmholtz Association; grant number VH-NG-
- 1031. Parts of the work were supported by the European Research Council under grant agreements
- Y. ERC-StG: 311552 (G.G.W.) and by the Deutsche Forschungsgemeinschaft (DFG) through the TUM
- International Graduate School of Science and Engineering (IGSSE, project BIOMAG; G.G.W., S.P.). This
- project has received funding from the European Union's Horizon 2020 research and innovation
- programme under grant agreement No. 823717-ESTEEM3.
- **Acknowledgments:** We thank D. Schmitz (Helmholtz-Zentrum Berlin (HZB) for fruitful collaboration.
- Yo We thank K.A. Mazzio (EM-ISPEK, HZB) for experimental support that helped us to synthesize and

- decorate the nanoparticles. We thank M. Kashefi (Ferdowsi University of Mashhad) for initiating the
- work on heterodimer structures and continuous support. We thank HZB and the Max Plank Society for
- the provision of access to the Energy Materials In-Situ Laboratory (EMIL) facilities.
- **Conflicts of Interest:** The authors declare no conflict of interest.
- Supplementary Information Available: Complementary structural and microstructural
- characteristics, including hydrodynamic diameter, size distribution, polydispersity index, crystallite
- diameter and XRD patterns, magnetometry and SAR measurements at different magnetic field
- A amplitudes and repeated runs, as well as optimization details of bare-CFO and CFO-Pd nanoparticles,
- are available free of charge via the ELSEVIER Publishing.

N References

١.

- [1] S. Tong, C. A. Quinto, L. Zhang, P. Mohindra, G. Bao, Size-Dependent Heating of Magnetic Iron Oxide Nanoparticles, ACS
- Nano **2017**, 11, 6808.
- 15 [2] H. Huang, S. Delikanli, H. Zeng, D. M. Ferkey, A. Pralle, Remote control of ion channels and neurons through magnetic-
- field heating of nanoparticles, Nat. Nanotechnol. 2010, 5 (8), 1.
- [3] R. Chen, G. Romero, M. G. Christiansen, A. Mohr, P. Anikeeva, Wireless magnetothermal deep brain stimulation, *Science*
- **1 2015**, 347, 1477.
- 1 U. B. Shinde, S. E. Shirsath, S. M. Patange, S. P. Jadhav, K. M. Jadhav, V. L. Patil, Preparation and Characterization of
- 19 Co²⁺ Substituted Li–Dy Ferrite Ceramics, *Ceram. Int.* **2013**, 39 (5), 5227.
- [5] M. R. Ghazanfari, M. Kashefi, S. F. Shams, M. R. Jaafari, Perspective of Fe₃O₄ Nanoparticles Role in Biomedical
- Applications, *Biochem. Res. Int.* **2016**, 1. Doi: 10.1155/2016/7840161.
- [6] M. R. Ghazanfari, M. R. Jaafari, S. F. Shams, M. Kashefi, Design and Fabrication of Multifunctional Temperature-sensitive
- Magnetoliposomal Nanostructures, *Mater. Today Commun.* **2017**, 13, 102.
- 7 £ [7] R. Hergt, S. Dutz, Magnetic Particle Hyperthermia-Biophysical Limitations of a Visionary Tumour Therapy, J. Magn.
- Υο Magn. Mater. **2007**, 311, 187.
- [8] I. A. Brezovich, Low Frequency Hyperthermia: Capacitive and Ferromagnetic Thermoseed Methods, Med. Phys.
- YY Monograph. **1988**, 16, 82.

- 1 [9] C. Martinez-Boubeta, K. Simeonidis, A. Makridis, M. Angelakeris, O. Iglesias, P. Guardia, A. Cabot, L. Yedra, S. Estrade, F.
- Y Peiro, Learning From Nature to Improve the Heat Generation of Iron-Oxide Nanoparticles for Magnetic Hyperthermia
- Applications, Sci. Reports. 2013, 3, 1652.
- [10] S. F. Shams, M. R. Ghazanfari, C. Schmitz-Antoniak, Magnetic-Plasmonic Heterodimer Nanoparticles: Designing
- ^o Contemporarily Features for Emerging Biomedical Diagnosis and Treatments, *Nanomater.* **2019**, 9, 1, 97.
- [11] J. Guozhi, W. Peng, Z. Yanbang, C. Kai, Localized Surface Plasmon Enhanced Photothermal Conversion in Bi2Se3
- V Topological Insulator Nanoflowers, Sci. Reports. 2016, 6, 25884.
- A [12] S. Bharathiraja, N. Q. Bui, P. Manivasagan, M. S. Moorthy, S. Mondal, H. Seo, N. T. Phuoc, T. T. V. Phan, H. Kim, K. D.
- ⁹ Lee, et al. Multimodal Tumor-Homing Chitosan Oligosaccharide-Coated Biocompatible Palladium Nanoparticles for
- Photo-based Imaging and Therapy, Sci. Reports. 2018, 8, 500.
- 11 [13] A. Dumas, P. Couvreur, Palladium: A Future Key Player in the Nanomedical Field? Chem. Sci. 2015, 6 (4), 2153.
- 17 [14] Q. Ding, D. Liu, D. Guo, F. Yang, X. Pang, R. Che, N. Zhou, J. Xie, J. Sun, Z. Huang, et al. Shape Controlled Fabrication of
- Magnetite Silver Hybrid Nanoparticles with High Performance Magnetic Hyperthermia, *Biomater*. **2017**, 124, 35.
- 15 S. Ota, N. Yamazaki, A. Tomitaka, T. Yamada, Y. Takemura, Hyperthermia Using Antibody-Conjugated Magnetic
- Nanoparticles and its Enhanced Effect with Cryptotanshinone, *Nanomater.* **2014**, 4, 319.
- 17 [16] A. Hervault, N. T. K. Thanh, Magnetic Nanoparticle-based Therapeutic Agents for Thermo-chemotherapy Treatment of
- 1 Cancer, *Nanoscale*. **2014**, 6, 11553.
- 1 K. Hayashi, M. Nakamura, H. Miki, S. Ozaki, M. Abe, T. Matsumoto, W. Sakamoto, T. Yogo, K. Ishimura, Magnetically
- 19 Responsive Smart Nanoparticles for Cancer Treatment with a Combination of Magnetic Hyperthermia and Remote-Control
- Y · Drug Release, Theranostics. 2014, 4, 834.
- [18] S. Dutz, N. Buske, J. Landers, C. Gräfe, H, Wende, J. H. Clement, Biocompatible magnetic fluids of Co-doped iron oxide
- nanoparticles with tunable magnetic properties, *Nanomater*. **2020**, 10, 1, 1019.
- [19] S. M. Ansari, B. B. Sinha, K. R. Pai, S. K. Bhat, Y. R. Ma, D. Sen, Y. D. kolekar, C. V. Ramana, Controlled
- surface/intersurface structure and spin enabled superior properties and biocompatibility of cobalt ferrite nanoparticles,
- Yo App. Surf. Sci. **2018**, 459, 788.
- [20] M. Ravichandran, G. Oza, S. Velumani, J. T. Ramirez, F. G. Sierra, ND. I. G. Gutierrez, R. Asomoza, One-dimensional
- ordered growth of magneto-crystalline and biocompatible cobalt ferrite nano-needles, *Matter. Let.* **2014**, 135, 67.
- YA [21] A. Sunny, A. kumar, V. Karunakaran, M. Athira, G. R. Mutta, K. K. Maiti, V. R. Reddy, M. Vasundhara, Magnetic
- rg properties of biocompatible CoFe2O4 nanoparticles using a facile synthesis, Nano Struct. Nano Obj. 2018, 16, 69.
- (22] K. Laznev, D. Tzerkovsky, K. Kekalo, G. Zhavnerko, V. Agabekov, Iron-Cobalt Ferrite Nanoparticles—Biocompatibility
- and Distribution After Intravenous Administration to Rat, IEEE T. Magn., 2013, 49, 1.

- 1 [23] M. Lickmichand, C. S. Shaji, N. Valarmati, A. S. Benjamin, R. K. A. Kumar, S. Nayak, et al, *In vitro* biocompatibility and
- hyperthermia studies on synthesized cobalt ferrite nanoparticles encapsulated with polyethylene glycol for biomedical
- applications, *Materials Today: Proceedings*, **2019**, 15, 252-261.
- [24] P. C. Morais, R. L. Santos, A. C. M. Pimenta, R. B. Avezedo, E. C. D. Lima, Preparation and characterization of ultra-stable
- biocompatible magnetic fluids using citrate-coated cobalt ferrite nanoparticles, *Thin Solid Films*, **2006**, **515**, 266-270.
- [25] N. Sanpo, C. C. Berndt, C. Wen, J. Wang, Transition metal-substituted cobalt ferrite nanoparticles for biomedical
- v applications, *Acta Biomater.*, **2013**, 9, 5830-5837.
- A [26] M. S. Seehra, J. D. Rall, J. C. Liu, C. B. Roberts, Core-Shell Model for the Magnetic Properties of Pd Nanoparticles,
- 9 *Mater. Lett.* **2012**, 68, 347.
- 1. [27] T. Huang, J. Cheng, Y. F. Zheng, In Vitro Degradation and Biocompatibility of Fe-Pd and Fe-Pt Composites Fabricated by
- Spark Plasma Sintering, Mater. Sci. Eng. C. 2014, 35, 43.
- 17 [28] J. Shen, Y. Zhu, X. Yang, J. Zong, C. Li, Multifunctional Fe₃O₄@Ag/SiO₂/Au Core-Shell Microspheres as a Novel SERS-
- activity Label via Long-range Plasmon Coupling, Langmuir. 2012, 29, 690.
- 15 [29] Z. Xu, Y. Hou, S. Sun, Magnetic Core/Shell Fe₃O₄/Au and Fe₃O₄/Au/Ag Nanoparticles with Tunable Plasmonic Properties,
- 10 J. Am. Chem. Soc. 2007, 129, 8698.
- [30] C. Yuen, Q. Liu, Optimization of Fe₃O₄@Ag Nanoshells in Magnetic Field Enriched Surface-Enhanced Resonance Raman
- NY Scattering for Malaria Diagnosis, *Analyst.* **2013**, 138, 6494.
- 1 B. H. Jun, M. S. Noh, J. Kim, G. Kim, H. Kang, M. S. Kim, Y. T. Seo, J. Baek, J. H. Kim, J. Park, et al., Multifunctional Silver-
- 19 Embedded Magnetic Nanoparticles as SERS Nanoprobes and their Applications, Small. 2010, 6, 119.
- 7. [32] X. X. Han, A. M. Schmidt, G. Marten, A. Fischer, I. M. Weidinger, P. Hildebrandt, Magnetic Silver Hybrid Nanoparticles
- for Surface-Enhanced Resonance Raman Spectroscopic Detection and Decontamination of Small Toxic Molecules, ACS
- YY Nano. **2013**, 7, 3212.
- Tr [33] T. Zheng, Q. Zhang, S. Feng, J. –J. Zhu, Q. Wang, H. Wang, Robust Nonenzymatic Hybrid Nanoelectrocatalysts for Signal
- Amplification Toward Ultrasensitive Electrochemical Cytosensing, J. Am. Chem. Soc. 2014, 136, 2288.
- 134] H. Gu, Z. Yang, J. Gao, C. K. Chang, B. Xu, Heterodimers of Nanoparticles: Formation at a Liquid-Liquid Interface and
- 77 Particle-Specific Surface Modification by Functional Molecules, J. Am. Chem. Soc. 2005, 127, 34.
- [35] M. R. Buck, J. F. Bondi, R. E. Schaak, A Total-Synthesis Framework for the Construction of High-Order Colloidal Hybrid
- YA Nanoparticles, Nat. Chem. 2012, 4, 37.
- ⁷⁹ [36] J. Huang, Y. Sun, S. Huang, K. Yu, Q. Zhao, F. Peng, H. Yu, H. Wang, J. Yang, Crystal Engineering and SERS Properties of
- Ag-Fe₃O₄ Nanohybrids: From Heterodimer to Core-Shell Nanostructures, *J. Mater. Chem.* **2011**, 21, 17930.

- 1 [37] Y. Zhai, L. Han, P. Wang, G. Li, W. Ren, L. Liu, E. Wang, S. Dong, Superparamagnetic Plasmonic Nanohybrids: Shape-
- Controlled Synthesis, Tem-Induced Structure Evolution, and Efficient Sunlight-Driven Inactivation of Bacteria, ACS Nano.
- **2011**, 5, 8562.
- [38] Y. Chen, N. Gao, J. Jiang, Surface Matters: Enhanced Bactericidal Property of Core-Shell Ag-Fe₂O₃ Nanostructures to
- their Heteromer Counterparts from One-pot Synthesis, *Small.* **2013**, 9, 3242.
- [39] S. F. Shams, M. Kashefi, C. Schmitz-Antoniak, Statistical Approach of Synthesize CoFe₂O₄ Nanoparticles to Optimize
- their Characteristics using Response Surface Methodology, J. Magn. Magn. Mater. 2017, 432, 362.
- A [40] S. F. Shams, M. Kashefi, C. Schmitz-Antoniak, Rietveld Structure Refinement to Optimize the Correlation between Cation
- 9 Disordering and Magnetic Features of CoFe₂O₄ Nanoparticles, *New J. Chem.* **2018**, 42, 3050.
- 1. [41] A. Kovacs, R. Schierholz, K. Tillmann, K. FEI Titan G2 80-200 CREWLEY, J. Large-Scale Res. Facil. JLSRF 2016, 2, A43.
- [42] G. Vallejo-Fernandez, O. Whear, A. G. Roca, S. Hussain, J. Timmis, V. Patel, K. O'Grady, Mechanisms of Hyperthermia in
- Magnetic Nanoparticles, J. Phys. D: Appl. Phys. 2013, 46, 312001.
- 17 [43] R. E. Rosensweig, Heating Magnetic Fluid with Alternating Magnetic Field, J. Magn. Magn. Mater. 2002, 252, 370.
- 15 [44] Y. Feng, N. Panwar, D. J. H. Tng, S. C. Tjin, K. Wang, K. T. Yong, K. T. The Application of Mesoporous Silica Nano- Particle
- Family in Cancer Theranostics, Coord. Chem. Rev. 2016, 319, 86.
- [45] A. G. Kolhatkar, A. C. Jamison, D. Litvinov, R. C. Willson, T. R. Lee, Tuning the Magnetic Properties of Nanoparticles, *Int.*
- 1 J. Mol. Sci. 2013, 14, 15977.
- 1A [46] G. Kandasamy, A. Sudame, P. Bhati, A. Chakrabarty, S. N. Kale, D. Maity, Systematic Magnetic Fluid Hyperthermia
- 19 Studies of Carboxyl Functionalized Hydrophilic Superparamagnetic Iron Oxide Nanoparticles based Ferrofluids, J. Colloid
- Y . Interface Sci. **2018**, 514, 534.
- [47] F. Shubitidze, K. Kekalo, R. Stigliano, I. Baker, Magnetic Nanoparticles with High Specific Absorption Rate of
- Fig. 177 Electromagnetic Energy at Low Field Strength for Hyperthermia Therapy, J. App. Phys. 2015, 117, 094302.
- [48] M. R. Barati, C. Selomulya, K. Suzuki, Particle Size Dependence of Heating Power in MgFe₂O₄ Nanoparticles for
- Υ ٤ Hyperthermia Therapy Application, J. App. Phys. **2014**, 115, 17B522.
- To [49] T. E. Torres, E. Lima, A. Mayoral, A. Ibarra, C. Marquina, M. R. Ibarra, G. F. Goya, Validity of the Néel -Arrhenius Model
- for Highly Anisotropic Co_xFe_{3-x}O₄ Nanoparticles, *J. App. Phys.* **2015**, 118, 183902.
- [50] C. Tannous, J. Gieraltowski, The Stoner–Wohlfarth Model of Ferromagnetism, Eur. J. Phys. 2008, 29 (3), 475.
- YA [51] N. A. Spaldin, Magnetic Materials: Fundamentals and Device Applications; Cambridge University Press, New York, 2003.
- ⁷⁹ [52] S. Xu, Y. Ma, B. Geng, X. Sun, M. Wang, The Remanence Ratio in CoFe₂O₄ Nanoparticles with Approximate single
- T. Domain Sizes, Nanoscale Res. Lett. 2016, 11, 471.

- 1 [53] Y. Gromova, V. G. Maslov, M. A. Baranov, R. Serrano-García, V. A. Kuznetsova, F. Purcell-Milton, Y. K. Gunko, A. V.
- T Baranov, A. V. Fedorov, Magnetic and Optical Properties of Isolated and Aggregated CoFe₂O₄ Superparamagnetic
- Nanoparticles Studied by MCD Spectroscopy, J. Phys. Chem. C. 2018, 122, 22, 11491.
- [54] B. B. Lahiri, T. Muthukumaran, J. Philip, Magnetic Hyperthermia in Phosphate Coated Iron Oxide Nanofluids, J. Magn.
- o Magn. Mater. **2016**, 407, 101.
- [55] C. Guibert, V. Dupuis, V. Peyre, J. Fresnais, Hyperthermia of Magnetic Nanoparticles: Experimental Study of the Role of
- V Aggregation, J. Phys. Chem. C. **2015**, 119, 28148.
- A [56] B. B. Lahiri, S. Ranoo, J. Philip, Magnetic Hyperthermia Study in Water based Magnetic Fluids Containing TMAOH
- ⁹ Coated Fe₃O₄ using Infrared Thermography, *Infrared Phys. Technol.* **2017**, 80, 71.
- 1. [57] D. Maity, D. C. Agrawal, Synthesis of Iron Oxide Nanoparticles under Oxidizing Environment and their Stabilization in
- Aqueous and Non-aqueous Media, J. Magn. Magn. Mater. 2007, 308, 46.
- 17 [58] M. Woinska, J. Szczytko, A. Majhofer, J. Gosk, K. Dziatkowski, A. Twardowski, Magnetic Interactions in an Ensemble of
- Cubic Nanoparticles: A Monte Carlo Study, Phys. Rev. B. 2013, 88, 144421.
- 159] S. T. Xu, Y. Q. Ma, Y. F. Xu, X. Sun, B. Q. Geng, G. H. Zheng, Z. X. Dai, Pure Dipolar-Interacted CoFe₂O₄ Nanoparticles and
- their Magnetic Properties, *Mater. Res. Bull.* **2015**, 62, 142.
- [60] F. L. Zan, Y. Q. Ma, Q. Ma, Y. F. Xu, Z. X. Dai, G. H. Zheng, M. Z. Wu, G. Li, Magnetic and Impedance Properties of
- Nanocomposite CoFe₂O₄/Co_{0.7}Fe_{0.3} and Single Phase CoFe₂O₄ *via* One-step Hydrothermal, *J. Am. Ceram. Soc.* **2013**, 96, 3100.
- 1 [61] F. L. Zan, Y. Q. Ma, Q. Ma, G. H. Zheng, Z. X. Dai, M. Z. Wu, G. Li, Z. O. Sun, X. S. Chen, One-step Hydrothermal Synthesis
- and Characterization of High Magnetization CoFe₂O₄/Co_{0.7}Fe_{0.3} Nanocomposite Permanent Magnets, J. Alloy Compd. **2013**,
- Y 553, 79.
- [62] N. Adeela, K. Maaz, U. Khan, S. Karim, A. Nisar, M. Ahmad, G. Ali, X. F. Han, J. L. Duan, J. Liu, Influence of Manganese
- Substitution on Structural and Magnetic Properties of CoFe₂O₄ Nanoparticles, *J. Alloy Compd.* **2015**, 639, 533.
- [63] B. Q. Geng, Z. L. Ding, Y. Q. Ma, Unraveling the Correlation between the Remanence Ratio and the Dipolar Field in
- Magnetic Nanoparticles by Tuning Concentration, Moment, and Anisotropy, Nano Res. 2016, 9 (9), 2772.
- (64] A. Hillion, A. Tamion, F. Tournus, O. Gaier, E. Bonet, C. Albin, V. Dupuis, Advanced Magnetic Anisotropy Determination
- through Isothermal Remanent Magnetization of Nanoparticles, *Phys. Rev. B.* **2013**, 88, 094419.
- [65] K. Mazz, M. Usman, S. Karim, A. Mumtaz, S. K. Hasanain, M. F. J. Bertino, Magnetic Response of Core-Shell Cobalt
- Ferrite Nanoparticles at Low Temperature, J. Appl. Phys. **2001**, 105, 13917.
- ⁷⁹ [66] A. Ceylan, S. K. Hasanain, S. I. Shah, Experimental Observations of Field Dependent Activation of Core and Surface Spins
- in Ni-Ferrite Nanoparticles, J. Phys. Condens. Matter. 2008, 20, 195208.
- [67] D. Peddis, C. Cannas, G. Piccaluga, E. Agostinelli, D. Fiorani, Spin-Glass Like Freezing and Enhanced Magnetization in
- Ultra-small CoFe₂O₄ Nanoparticles, *Nanotechnol.* **2010**, 21, 125705.

- 1 [68] V. Blanco-Gutierrez, M. Virumbrales, R. Saez-Puche, J. Maria, Superparamagnetic Behavior of MFe₂O₄ Nanoparticles
- ^γ and MFe₂O₄/SiO₂ Composites (M: Co, Ni), J. Phys. Chem. C. **2013**, 117, 20927.
- [69] S. Laureti, G. Varvaro, A. M. Testa, D. Fiorani, E. Agostinelli, G. Piccaluga, A. Musinu, A. Ardu, D. Peddis, Magnetic
- Interactions in Silica Coated Nanoporous Assemblies of CoFe₂O₄ Nanoparticles with Cubic Magnetic Anisotropy,
- Nanotechnol. 2011, 21, 315701.
- [70] J. Mohapatra, F. Zeng, K. Elkins, M. Xing, M. Ghimire, S. Yoon, S. R. Mishra, J. P. Liu, Size-Dependent Magnetic and
- V Inductive Heating Properties of Fe₃O₄ Nanoparticles: Scaling Laws Across the Superparamagnetic Size, Phys. Chem. Chem.
- A Phys. **2018**, 20, 12879.
- ⁹ [71] V. Mameli, A. Musinu, A. Ardu, G. Ennas D. Peddis, D. Niznansky, C. Sangregorio, C. Innocenti, N. T. K. Thanh, C. Cannas,
- 1. Studying the Effect of Zn-Substitution on the magnetic and Hyperthermic Properties of Cobalt Ferrite Nanoparticles,
- Nanoscale. **2016**, 8, 10124.
- 17 [72] F. Bensebaa, F. Zavaliche, P. LEcuyer, R. W. Cochrane, T. Veres, Microwave Synthesis and Characterization of Co-Ferrite
- Nanoparticles, J. Colloid Interface Sci. 2004, 277, 104.
- 15 [73] H. M. K. Tedjieukeng, P. K. Tsobnang, R. L. Fomekong, E. P. Etape, P. A. Joy, A. Delcortee, J. N. Lambi, Structural
- 10 Characterization and Magnetic Properties of Undoped and Copper-doped Cobalt Ferrite Nanoparticles Prepared by the
- Octanoate Coprecipitation Route at Very Low Dopant Concentrations, RSC Adv. 2018, 8, 38621.
- [74] I. Morales, R. costo, N. Mille, G. B. da Silva, J. Carrey, A. Hernando, P. de la Presa, High Frequency Hysteresis Losses on
- Fe2O3 And Fe3O4: Susceptibility as a Magnetic Stamp for Chain Formation, Nanomater. 2018, 8, 970;
- 19 doi:10.3390/nano8120970.
- 7. [75] Z. Nemati, J. Alonso, I. Rodrigo, R. Das, E. Garaio, J. A. Garcia, I. Orue, M. –H. Phan, H. Srikanth, Improving the Heating
- Efficiency of Iron Oxide Nanoparticles by Tuning Their Shape and Size, J. Phys. Chem. C, 2018, 122, 2367.
- [76] E. Garaio, O. Sandre, J. –M. Collantes, J. A. Garcia, S. Mornet, F. Plazaola, Specific absorption rate dependence on
- temperature in magnetic field hyperthermia measured by dynamic hysteresis losses (ac magnetometry), Nanotechnology,
- ۲٤ **2015**, 26, 015704.
- To [77] N. Waldoefner, K. Stief, K. Magnetic transducers. US patent, MAGFORCE AG (Berlin), 2017, Patent number: 9814677.
- [78] I. Andreu, E. Natividad, C. Ravagli, M. Castro, G. Baldi, Heating Ability of Cobalt Ferrite Nanoparticles Showing Dynamic and
- YV Interaction Effects, RSC Adv. 2014, 4, 28968.
- [79] S. Laurent, S. Dutz, U. O. Häfeli, M. Mahmoudi, Magnetic Fluid Hyperthermia: Focus on Superparamagnetic Iron Oxide
- Nanoparticles, Adv. Colloid Interface Sci. 2011, 166, 8.

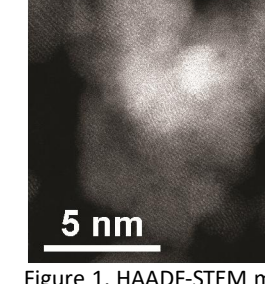
Table 1. Static magnetic characteristics of CFO nanoparticles with different hydrodynamic diameters d_H and corresponding CFO-Pd heterodimers extracted from field-dependent magnetization measurements at 300 K.

Composition	d _H (nm)	M _s (kA/m)	K _{eff} (10 ⁵ J/m ³)	Xmax		
CFO	7.20	37 ± 8	0.4 ± 0.1	0.6 ± 0.1		
CFO	24.10	72 ± 11	1.5 ± 0.3	$\textbf{0.74} \pm \textbf{0.1}$		
CFO-Pd	7.20	160 ± 20	2.7 ± 0.4	1.8 ± 0.2		
CFO-Pd	24.10	145 ± 20	2.9 ± 0.4	1.5 ± 0.2		

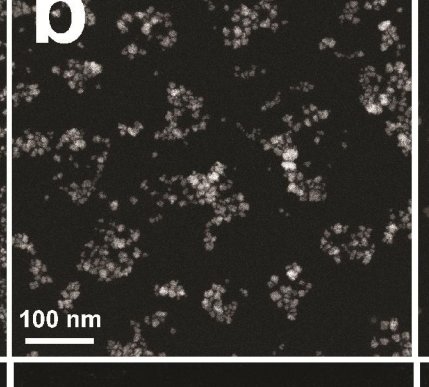
١.

Table 2. Optimized synthesis parameters and structural characteristics to achieve maximum size-dependent SAR values.

Response	Target	Factor	Value	Conditions	Response values
SAR (W/g _{CFO})	Maximize	Temperature (°C)	105	Dantialas sias 42 22 mm	78.205 ± 3.12
		рН	10.61	Particles size: 13.32 nm Size distribution: 4.56 nm	
		Cation ratio	0.52	312e distribution: 4.36 mm	
SAR (W/g _{CFO})	Maximize	Crystallite size (nm)	12.67		76.48 ± 2.29
		Crystallinity (%)	76.32	All factors in range	
		X _B -X _A	0.45		



200 nm



е

3 nm



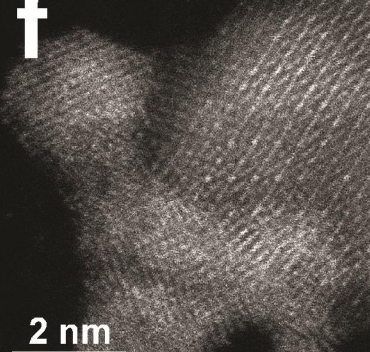


Figure 1. HAADF-STEM micrographs of 7.20 nm CFO-Pd heterodimers. The mean sizes of the CFO and Pd nanoparticles are approximately 7 and 2 nm, respectively, with a PDI value of 0.07.



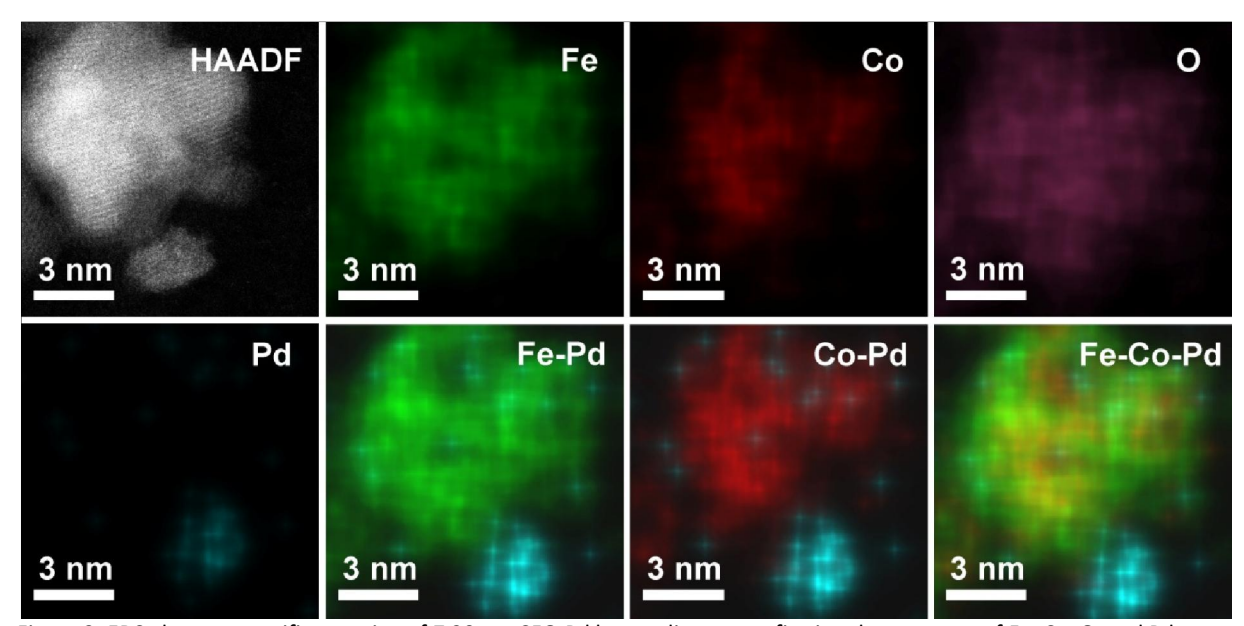
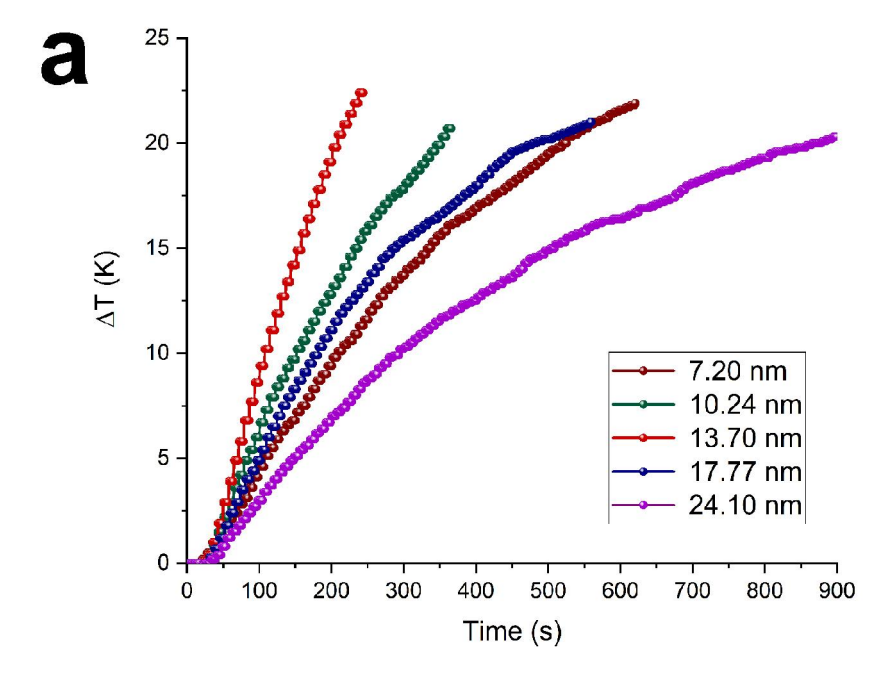


Figure 2. EDS element-specific mapping of 7.20 nm CFO-Pd heterodimers, confirming the presence of Fe, Co, O, and Pd.



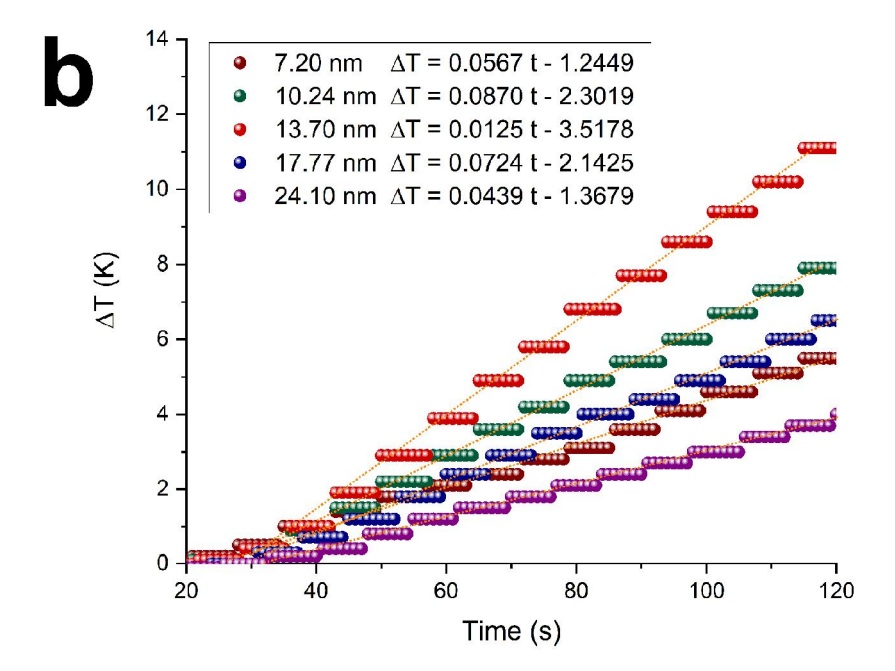
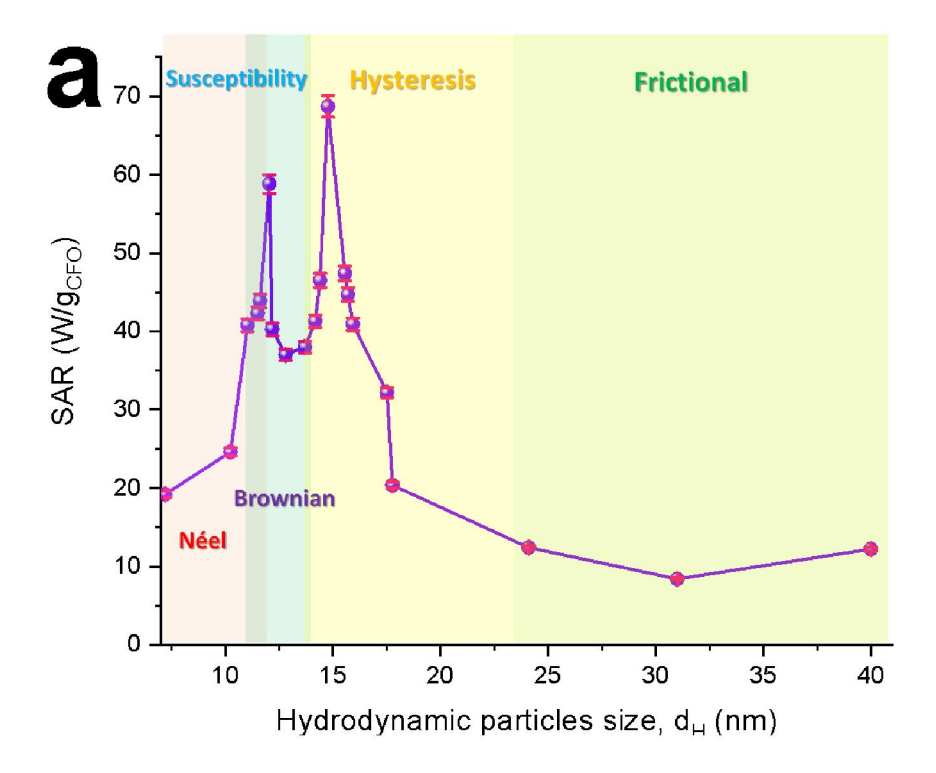


Figure 3. (a) Temperature variation plotted as a function of time $\Delta T/\Delta t$ for CFO ferrofluids with different particle sizes, and (b) initial slopes of the $\Delta T/\Delta t$ curves and associated fitted linear equations used to calculate SAR values. The fluid concentration, magnetic field amplitude and frequency were 15 mg/ml, 19 mT and 318 kHz, respectively. The error in the $\Delta T/\Delta t$ measurements was estimated to be approximately 2%.



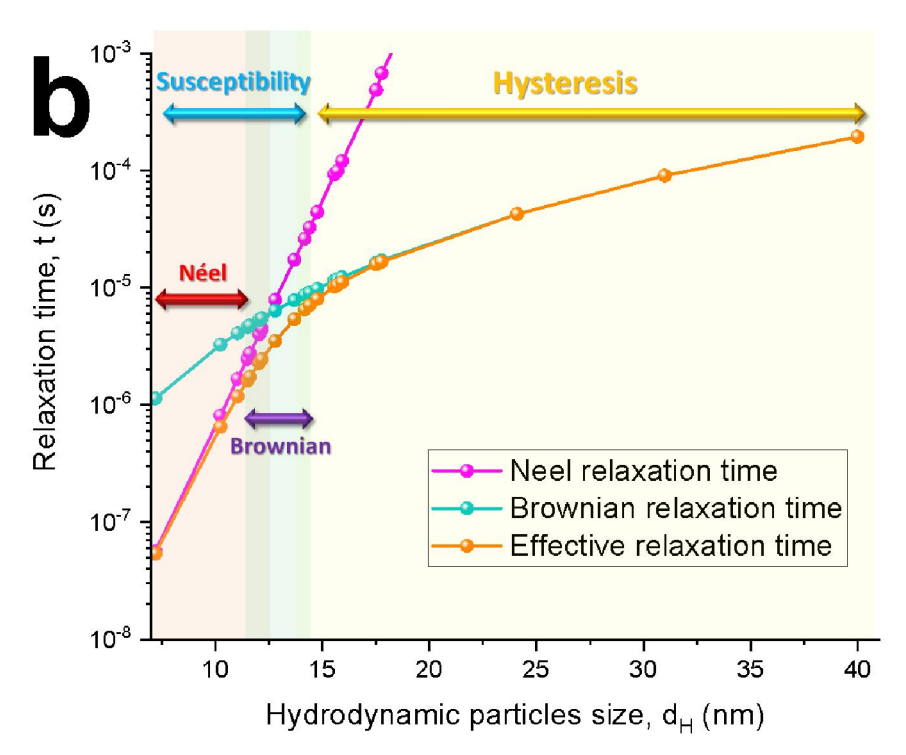


Figure 4. (a) SAR variation for CFO ferrofluids plotted as a function of particles size, and (b) curves of Néel, Brownian, and effective relaxation time plotted as a function of particle size for CFO nanoparticle suspensions. The fluid concentration, magnetic field amplitude and frequency were 15 mg/ml, 19 mT and 318 kHz, respectively. The error in the SAR measurements was estimated to be approximately 2%.

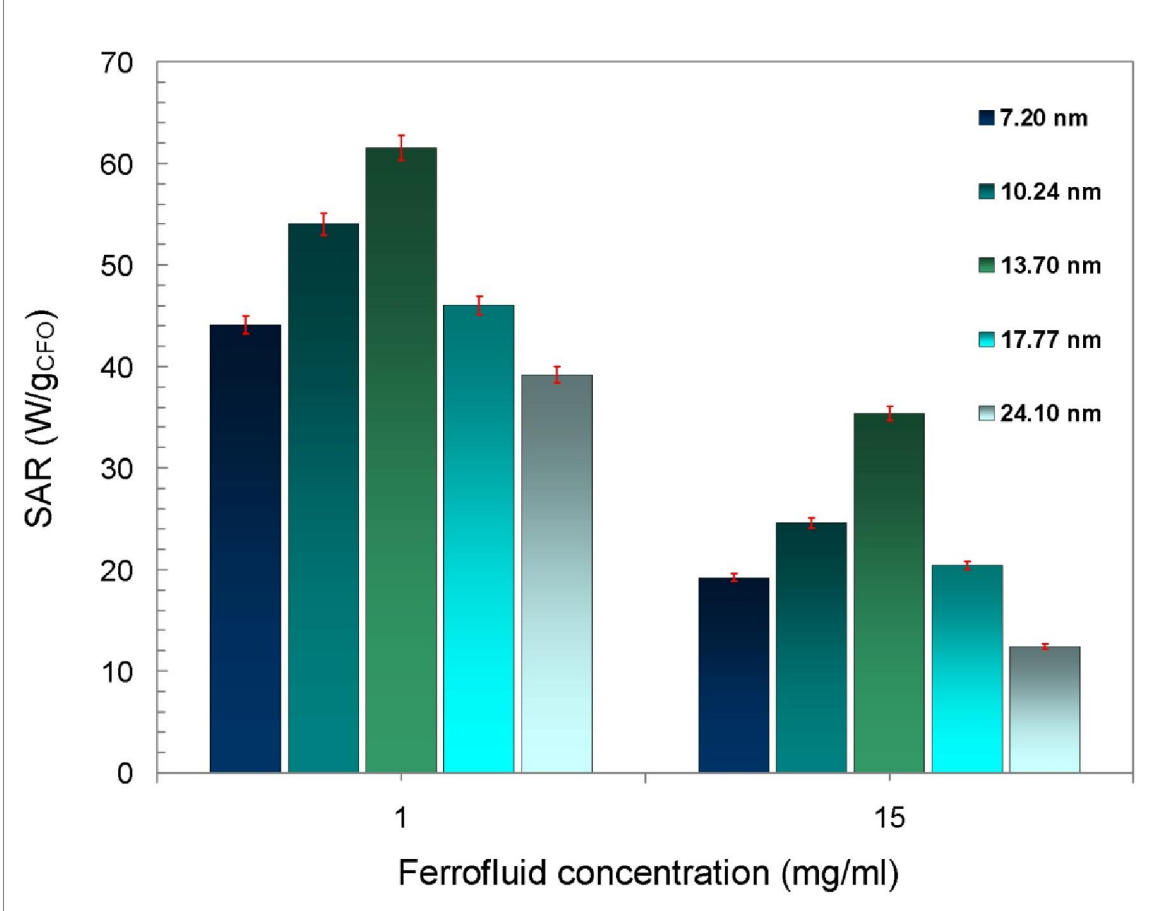


Figure 5. SAR values of CFO nanoparticle suspensions with concentration levels of 1 and 15 mg/ml for five different particle sizes. In all of the samples, the SAR values are higher for the lower-concentration fluids than for the higher-concentration suspensions. The magnetic field amplitude and frequency were 19 mT and 318 kHz, respectively. The error in the SAR measurements was estimated to be approximately 2%.

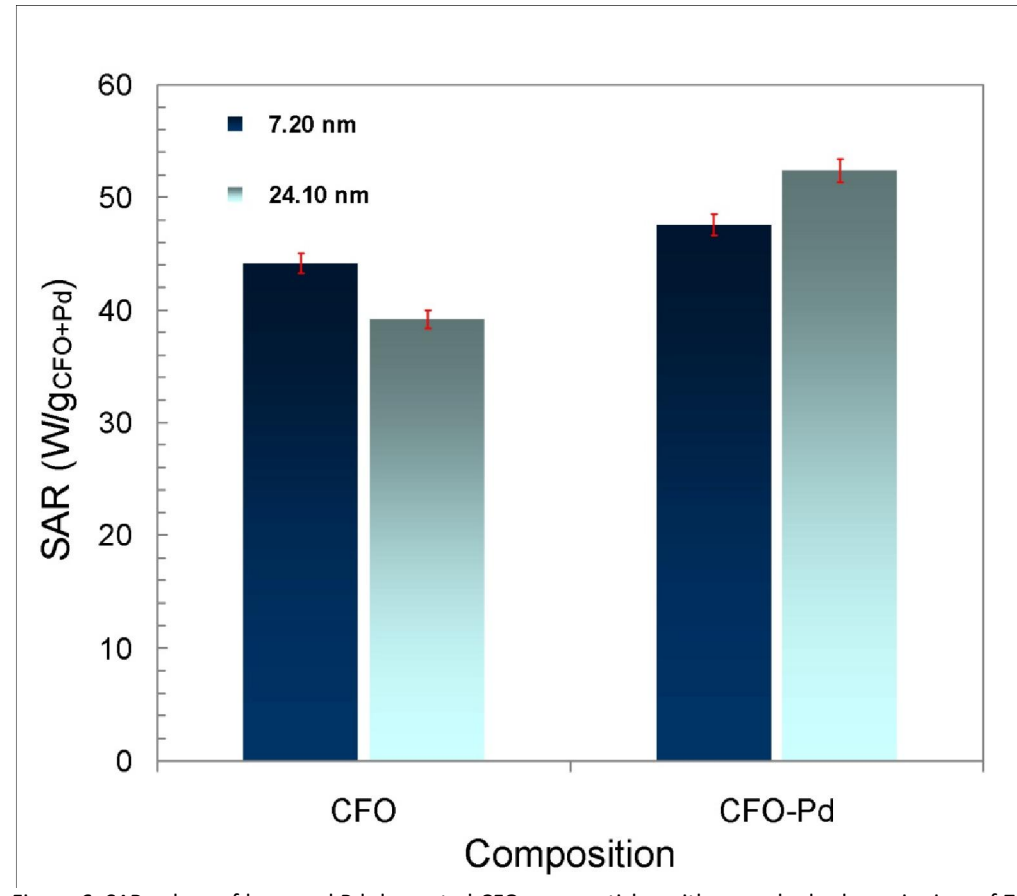


Figure 6. SAR values of bare and Pd-decorated CFO nanoparticles with mean hydrodynamic sizes of 7.20 and 24.10 nm. In both samples, the calculated SAR values increase significantly after Pd decoration. The fluid concentration, magnetic field amplitude and frequency were 1 mg/ml, 19 mT and 318 kHz, respectively. The error in the SAR measurements was approximately 2%.

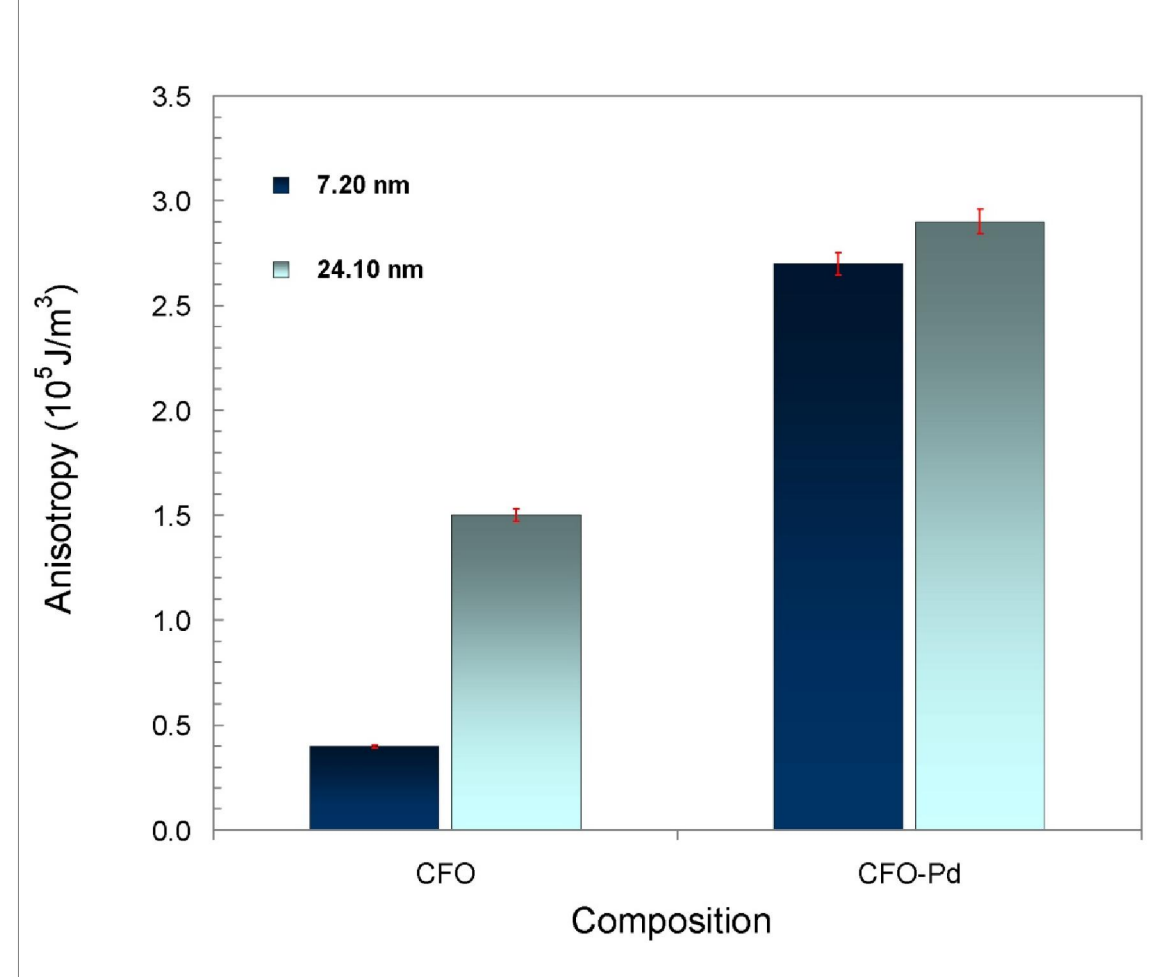


Figure 7. Magnetic anisotropy values of bare and Pd-decorated CFO nanoparticles with mean hydrodynamic sizes of 7.20 and 24.10 nm determined from field-dependent magnetization measurements performed at 300 K. The error in the SAR measurements was approximately 2%.

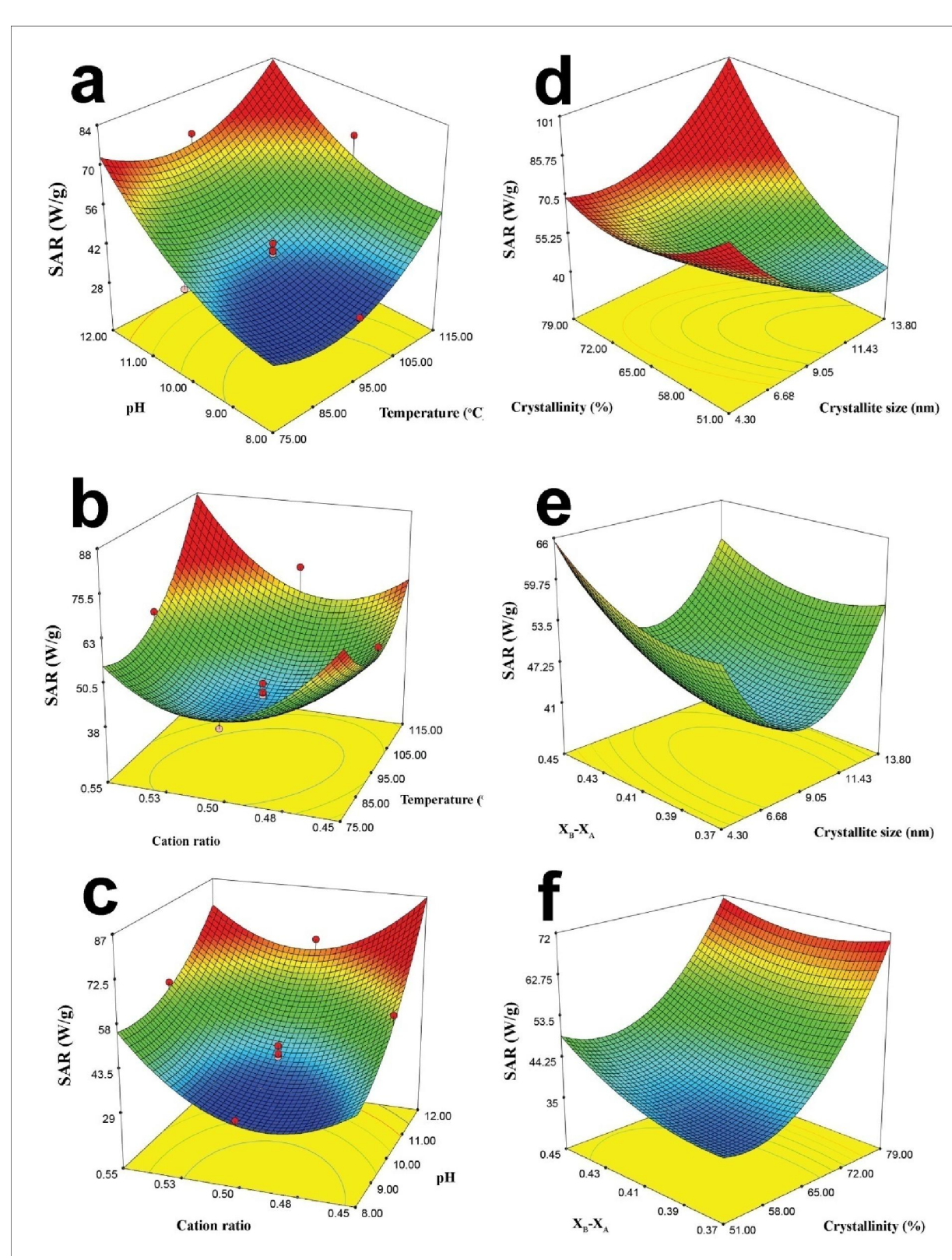


Figure 8. (a-c) SAR value variation plotted as a function of synthesis parameters: (a) reaction temperature and pH at a Co^{2+}/Fe^{3+} cation ratio of 0.50; (b) reaction temperature and cation ratio at a pH of 11; (c) pH and cation ratio at a temperature of 95 °C. (d-f) SAR value variation plotted as a function of structural characteristics: (d) crystallite size and crystallinity at a cation distribution factor (X_B - X_A) of 0.42; (e) crystallite size and cation distribution at a crystallinity of 76%; (f) crystallinity and cation distribution at a crystallite size of 13.5 nm. The SAR values were calculated from measurement results. The fluids concentration, magnetic field amplitude and frequency were 15 mg/ml, 19 mT, and 318 kHz, respectively. The error bar was estimated to be approximately 4% in (a-c) and 3% in (d-f) using a predictive model.

Graphical Abstract

